12-1-2005

Structural Allostery and Binding of the Transferrin·Receptor Complex

Guozhong Xu
Case Western Reserve University

Mark R. Chance
Case Western Reserve University, mark.chance@case.edu

Author(s) ORCID Identifier:

Mark R. Chance

Recommended Citation
Guozhong Xu, Rutao Liu, Olga Zak, Philip Aisen, Mark R. Chance. Structural Allostery and Binding of the Transferrin·Receptor Complex. Molecular & Cellular Proteomics, Volume 4, Issue 12, 2005, Pages 1959-1967, https://doi.org/10.1074/mcp.M500095-MCP200.

Structural Allostery and Binding of the Transferrin·Receptor Complex*

Guozhong Xu‡§, Rutao Liu§¶, Olga Zak¶, Philip Aisen¶, and Mark R. Chance‡‖

The structural allostery and binding interface for the human serum transferrin (Tf)·transferrin receptor (TfR) complex were identified using radiolytic footprinting and mass spectrometry. We have determined previously that the transferrin C-lobe binds to the receptor helical domain. In this study we examined the binding interactions of full-length transferrin with receptor and compared these data with a model of the complex derived from cryoelectron microscopy (cryo-EM) reconstructions (Cheng, Y., Zak, O., Aisen, P., Harrison, S. C. & Walz, T. (2004) Structure of the human transferrin receptor·transferrin complex. *Cell* 116, 565–576). The footprinting results provide the following novel conclusions. First, we report characteristic oxidations of acidic residues in the C-lobe of native Tf and basic residues in the helical domain of TfR that were suppressed as a function of complex formation; this confirms ionic interactions between these protein segments as predicted by cryo-EM data and demonstrates a novel method for detecting ion pair interactions in the formation of macromolecular complexes. Second, the specific side-chain interactions between the C-lobe and N-lobe of transferrin and the corresponding interactions sites on the transferrin receptor predicted from cryo-EM were confirmed in solution. Last, the footprinting data revealed allosteric movements of the iron binding C- and N-lobes of Tf that sequester iron as a function of complex formation; these structural changes promote tighter binding of the metal ion and facilitate efficient ion transport during endocytosis. *Molecular & Cellular Proteomics 4: 1959–1967, 2005.*

The transferrin (Tf)[1]·transferrin receptor I (TfR) complex has received considerable attention because of its role in cellular iron uptake, which is crucial for a broad range of cellular processes (1–7). TfR is a homodimer and type II transmembrane glycoprotein capable of binding two molecules of transferrin, a bilobal iron-carrying glycoprotein. TfR serves as a gatekeeper in regulating cellular iron uptake due to its selective binding of iron-bearing Tf at the slightly basic pH of the cell surface; this binding is followed by endocytosis and iron release in the acidic endosome (1). Apotransferrin remains bound to TfR at endosomal pH and is transported back to the cell surface where the transition to a slightly basic pH triggers the dissociation of the complex.

Although high resolution crystal structures of Tf (8) and TfR (6) have been available for some time, no crystallographic structure of any Tf·TfR complex has been reported. Recently Cheng *et al.* (3) obtained an atomic model of the human Tf·TfR complex by docking the crystal structures of human TfR ectodomain and iron-loaded N-terminal and C-terminal lobes of Tf into a 7.5-Å resolution density map generated by cryoelectron microscopy (cryo-EM) image reconstruction and single particle averaging techniques. Although the moderate resolution of the cryo-EM images (compared with atomic resolution x-ray data) does not permit identification of individual residues and side chains of the proteins, the contours in this case are sufficiently well defined to allow unambiguous orientations in docking of the crystal structures into the electron density map. Side-chain interactions are then inferred from the overlaid crystal structures, and these proposed interactions have guided mutagenesis studies (3). The resulting model (Fig. 1) indicates that the Tf C-lobe binds laterally at the helical domain of TfR, and the Tf N-lobe is sandwiched between the TfR ectodomain and the cell membrane. Specific predictions as to points of side-chain contact can be made from this model. In particular, potential ion pair interactions between acidic residues in the Tf-C lobe and basic residues in the TfR helical domain that might mediate both specific as well as high affinity C-lobe binding to the helical domain were suggested (3, 9–11). Protein/protein interfaces for heteromeric complexes frequently contain charged and polar residues especially compared with the cores of proteins (12–17). However, the cryo-EM data are just suggestive with respect to the specific side chains involved, and methods to confirm protein/ligand interfaces and their charge-charge interactions are essential for understanding molecular recognition involving the specific and dynamic interactions of biological assemblies.

Oxidative footprinting coupled with mass spectrometry has been proven to be a powerful technique for examining protein structure and biological assemblies as well as ligand-dependent conformational changes (5, 18–26). The radiolytic oxidations of amino acid side chains (27–32) within the protein structure are examined by LC-MS and LC-MS/MS; ligand-de-

From the ‡Case Center for Proteomics and Mass Spectrometry, Case Western Reserve University, Cleveland, Ohio 44106 and the ¶Department of Physiology and Biophysics, Albert Einstein College of Medicine, Bronx, New York 10461

Received, April 4, 2005, and in revised form, September 14, 2005
Published, MCP Papers in Press, September 16, 2005, DOI 10.1074/mcp.M500095-MCP200

[1] The abbreviations used are: Tf, transferrin; TfR, transferrin receptor I; cryo-EM, cryoelectron microscopy; dTf, diferric transferrin; SASA, solvent-accessible surface area.

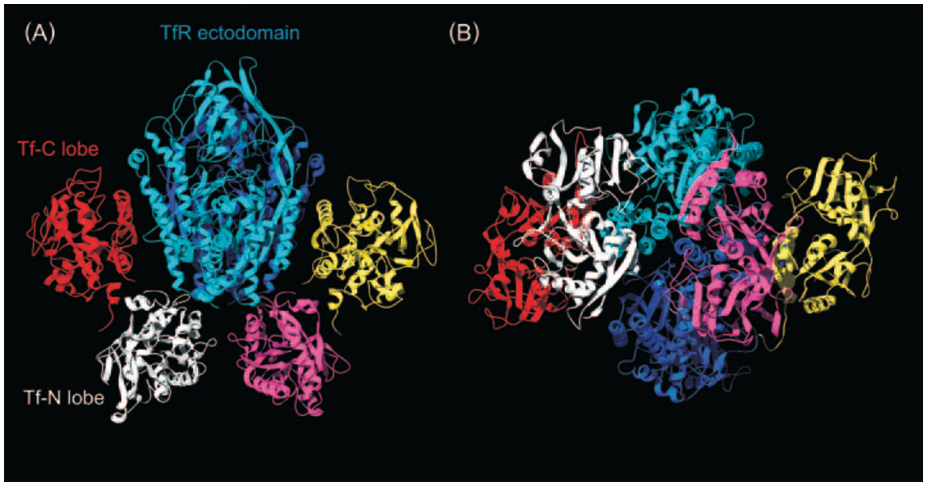

FIG. 1. **Cryo-EM model of diferric Tf·TfR (ectodomain) complex.** *A*, face-on view. *B*, bottom view.

pendent alternations of reactivity are interpretable in the context of known three-dimensional structure information. Using radiolytic footprinting, we previously examined the interactions of isolated Tf C-lobe with TfR (5). This confirmed that the Tf C-lobe binds to the receptor helical domain and induces allosteric changes in TfR remote from the binding site. In the present study, we examined the binding of full-length Tf to TfR. These data were then compared with the cryo-EM model of the complex to test specific hypotheses related to the contact surfaces in solution.

EXPERIMENTAL PROCEDURES

Sample Preparation—The soluble TfR ectodomain expressed in a baculovirus system was provided by Dr. Peter Snow at the California Institute of Technology. Lyophilized human diferric transferrin (dTf) was purchased from Roche Applied Science and shown to be homogeneous by SDS-PAGE and indistinguishable in its spectroscopic properties from native dTf isolated in this laboratory from Cohn fraction IV-7 (33). The dTf·TfR complex (2:2 stoichiometry) was prepared by incubating a 2-fold molar excess of dTf with about 10^{-4} M TfR subunits for 1 h at 37 °C and then overnight at 4 °C. The complex was separated from the uncomplexed components by size exclusion chromatography (10, 34). The complex is well resolved and can be cleanly isolated from the uncomplexed proteins. Based on $A_{280} = 1.2$, final concentrations of the 2:2 complex taken for synchrotron irradiation was estimated to be approximately 10^{-5} M.

Solvent-accessible Surface Area (SASA) Calculation—The VADAR 1.2 program (Protein Engineering Network of Center of Excellence, University of Alberta, Edmonton, Alberta, Canada) was used to calculate the solvent SASA of all side chains (Å^2) from human dTf C-lobe, N-lobe, and TfR dimer using a Protein Data Bank file of iron-loaded Tf C-lobe (provided by Dr. Harmon Zuccola) and Protein Data Bank codes 1N84 and 1CX8, respectively. For comparison, the protected side chains as a function of complex formation were also predicted from the cryo-EM model (Protein Data Bank 1SUV) (3) using Surface Racer 1.2 (35). In this calculation TfR was removed for calculating the SASA of isolated Tf, whereas Tf was removed for calculating the SASA of isolated TfR.

Synchrotron X-ray Radiolysis and LC-MS Analysis—Prior to radiolysis, dTf, TfR, and their complex were dialyzed against 20 mM sodium cacodylate buffer (pH 7.0) at 4 °C overnight (5). Samples were exposed to the synchrotron x-ray beam at the X28C beamline of National Synchrotron Light Source at Brookhaven National Laboratory (Upton, NY) for 0–300 ms in accordance with our established protocols (5, 20, 36). The irradiated samples were then reduced with 10 mM DTT (Roche Diagnostics) and denatured by adding 15% acetonitrile and heating at 95 °C for 25 min followed by cooling on ice. Digestion was performed using sequencing grade modified trypsin (Promega Biosciences, Madison, WI) and Asp-N (Roche Diagnostic) at 37 °C for 15–18 h. Peptide mixtures were separated by reverse phase HPLC using a C_{18} column and examined by ESI-MS and MS/MS, and data analysis was carried out according to our published procedures (5, 20).

RESULTS

Protections on Full-length Transferrin upon Receptor Binding—Human transferrin (1) consists of two globular lobes, the N-lobe and the C-lobe, joined by a flexible peptide strand (Fig. 2*A*). Each lobe is further divided into two domains (C1, C2, N1, and N2) separated by a deep interdomain cleft, which houses a high affinity yet reversible iron binding site. Tf C-lobe is the primary receptor recognition lobe, accounting for most of the binding energy of the Tf·TfR complex (3, 11). The sequences and rate constants for peptides of full-length Tf and TfR that experienced protection upon complex formation are listed in Table I. Dose-response curves for two selected peptides, Tf peptide 366–380 and TfR peptide 648–658, are displayed in Fig. 3, while those for the other peptides from Table I are shown in Supplemental Fig. 1. Many other peptides from Tf, TfR, and their complex were examined as well; none of them showed significant changes in oxidation rate constants as a function of complex formation and are not reported.

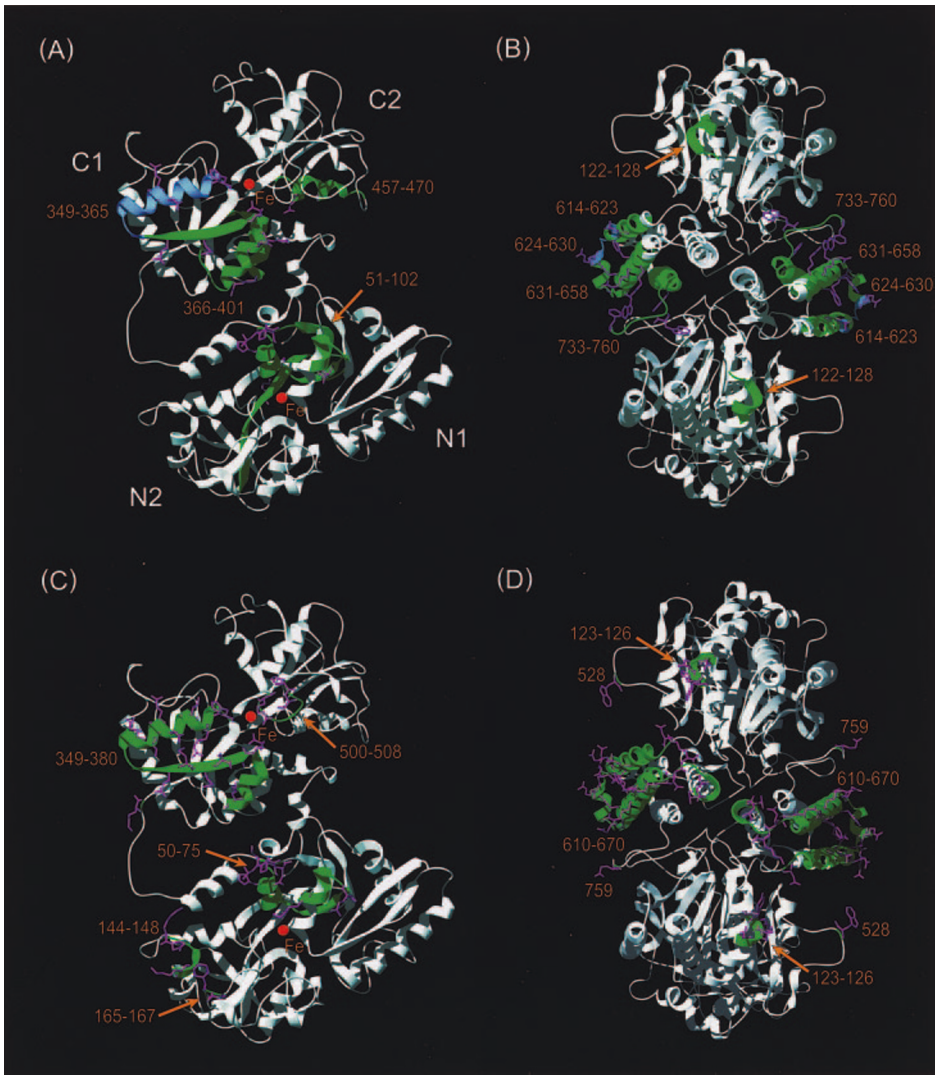

FIG. 2. **Protected and interfacial residues indicated on the structure of Tf (*A* and *C*) and TfR ectodomain (*B* and *D*).** The iron-loaded full-length rabbit Tf (8) is used to display the structure of Tf. In *A* and *B*, the peptide sequences showing reduced oxidation rates upon complex formation from Table I are shown for Tf (*A*) and the TfR dimer (*B*). The backbone positions of the peptide sequences are colored in *green*, and the side chains of the probe residues identified by tandem MS are colored in *purple*. In *C* and *D*, peptide segments indicated to be contact points between Tf and TfR are colored in *green*, and the specific side chains that are calculated to experience a reduction in SASA >15% are indicated in *purple*. *A*, footprinting data for full-length Tf. The protected residues include Val-60, Tyr-68, Tyr-71, Leu-72, Pro-74, Phe-94, and Tyr-96 in peptides 51–88 and 89–102; Glu-367, Val-369, Glu-372, Glu-375, and Asp-376 in peptide 366–380; Met-382 and Met-389 in peptide 381–401; and Trp-460 and Met-464 in peptide 457–470. Peptide 349–365 containing residues His-349, Asp-356, and Glu-357 is indicated to contribute to C-lobe contacts based on mutagenesis experiments; these residues are colored *blue*. *B*, footprinting data for TfR ectodomain. The probe residues include Leu-619 in peptide 614–623; Met-635, Trp-641, Tyr-643, Phe-650, Arg-651, and Arg-655 in peptide 631–658; and Trp-740, Trp-754, and Phe-760 in peptide 733–760. Peptide 624–630 containing Arg-629, which contributes to Tf binding as indicated by mutagenesis (9), is displayed in *blue*. *C*, solvent accessibility calculations of full-length Tf based on the cryo-EM model. The residues experiencing decreases in solvent accessible surface >15% as a function of complex formation include Arg-50, Glu-56, Tyr-68, Tyr-71, Leu-72, Ala-73, Pro-74, and Asn-75 in sequence 50–75; Lys-144, Pro-145, and Lys-148 in sequence 144–148; Thr-165 and Phe-167 in sequence 165–167; Lys-340; His-349, Arg-352, Leu-353, Asp-356, Glu-357, Ser-359, Val-360, Thr-361, Glu-367, Cys-368, Glu-369, Ser-370, Ala-371, Glu-372, and Lys-380 in sequence 349–380; and Pro-500, Ser-501, and Arg-508 in sequence 500–508. *D*, solvent accessibility calculations of TfR ectodomain based on the cryo-EM model. The interfacial residues include Tyr-123, Trp-124, Asp-125, and Asp-126 in sequence 123–126; Trp-528; Asp-610, Leu-619, Val-622, Arg-623, Asn-626, Gln-627, Arg-629, Gln-640, Tyr-643, Ser-644, Arg-646, Phe-650, Arg-651, Ser-654, Thr-658, Gly-661, Asn-662, Ala-663, Glu-664, Lys-665, Asp-667, and Val-670 in sequence 610–670; and Glu-759.

Table I shows the residue numbers and sequences for selected peptides from Tf or TfR; all the peptides shown are derived from trypsin digestions except two at the bottom of the table generated by Asp-N cleavages. The probe residues (*e.g.* the ones oxidized in the footprinting experiments) for each peptide were identified using tandem MS and are bold-

TABLE I

Peptides from transferrin and receptor that show significant changes in oxidation rate as a function of complex formation

Sequence	Peptide	Rate Constant (s^{-1})	
		Isolated Protein	Complex
Transferrin N-lobe (1-333) and C-lobe (334-679)			
51-88	A I A A N E A D A **V** T L D A G L V **Y** D A 7 24 **Y L A P** N N L K P V V A E F Y G S K 52 70 121	1.23±0.05	0.13±0.03
89-102	E D P Q T **F** Y **Y** A V A V V V K 68 16	1.7±0.2	0.14±0.09
366-380	I **E** C **V** S A **E** T T **E D** C I A K 67 35 72 20 44	0.37±0.02 0.50±0.02 †	0.20±0.02 0.08±0.02 †
381-401	I **M** N G E A D A **M** S L D G G F V Y I A G K 11 8	1.4±0.1	0.12±0.04
457-470	T A G **W** N I P **M** G L L Y N K 39 0.3	1.4±0.1	0.33±0.04
Receptor Protease-like (122-188) and Helical (607-760) Domains			
122-128	L **Y** **W** D D L K 170 47	1.6±0.2	1.0±0.2
614-623	Y N S Q L **L** S **F** V R 64 15	0.87±0.04	0.10±0.03
634-646	E **M** G L S L Q **W** L **Y** S A R 10 135 76	2.1±0.1	0.17±0.04
647-651	G D F **F** **R** 103 153	1.7±0.1	0.13±0.03
733-760#	N Q L A L A T **W** T I Q G A A N A L S G 5 D V **W** D I D N E **F** 211 84	0.90±0.06	0.18±0.04
631-647*	D I K E **M** G L S L Q **W** L **Y** S A R G 10 135 76	2.6±0.2	0.2±0.1
648-658*	D F **F** **R** A T S **R** L T T 103 153 74	1.6±0.1 0.63±0.08 ††	0.23±0.09 0.05±0.08 ††

† Rates for -30 Da products.

†† Rates for -43 Da products.

#-C-terminal peptide.

* From Asp-N digestion, while all other peptides from trypsin digestion.

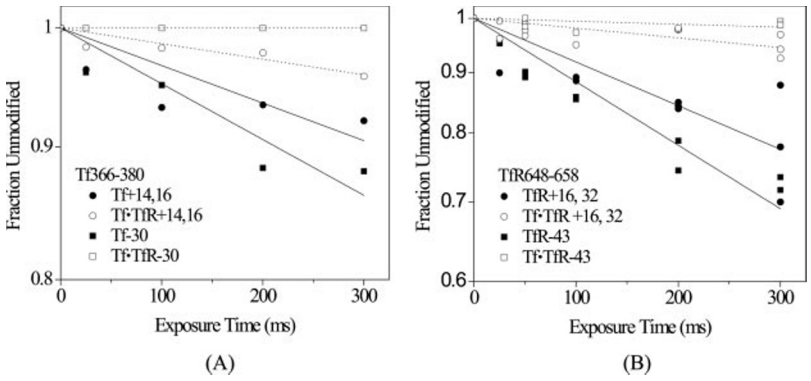

FIG. 3. **Dose-response curves for Tf peptide 366–380 (*A*) and TfR peptide 648–658 (*B*).** Data for the isolated proteins and Tf·TfR complex are shown and are described in the text. The data are fit according to the "Experimental Procedures," and the rate constants are shown in Table I.

faced. These probe sites are the reporter groups in the footprinting experiments and may experience increases, decreases, or no changes in oxidation rates as a function of complex formation. The SASAs of the specific probe side chains as calculated from the crystal structures of the isolated proteins are shown underneath the peptide sequences. Three

peptides within the Tf C-lobe and two peptides within the N-lobe experienced significant protections upon complex formation (Table I). The backbone segments of these peptides are colored in *green* on the structure of full-length Tf in Fig. 2*A*, and the peptide residue numbers are labeled as well to illustrate the positions of these peptides on the structure. The actual probe side-chain residues are colored in *purple*. Within the C-lobe, the protected peptides include sequences 366–380 and 381–401 from the C1 subdomain and peptide 457–470 from the C2 subdomain. In our previous analysis of C-lobe binding to TfR, we observed protections upon complex formation for peptides 381–401 and 457–470, indicating that the binding mode of isolated C-lobe is very similar to that seen for the C-lobe of full-length Tf. The present studies provide new data for the N-lobe in which peptides 51–88 and 89–102 experienced protections upon complex formation.

Oxidative Decarboxylation of Acidic Residues in Tf Is Suppressed upon Complex Formation—Dose-response curves of peptide 366–380 in the C1 domain are shown in Fig. 3*A*. This peptide experienced a ~2-fold decrease in the observed oxidation rate constant upon complex formation when the +14- and +16-Da oxidation products of valine were quantitated (Fig. 3*A*, *open versus closed circles*, and Table I). The peptide contains four acidic residues; recently we determined that solvent-accessible acidic residues are subject to oxidative decarboxylation. The decarboxylation is accompanied by aldehyde formation and results in a characteristic mass shift of −30 Da (29).

We examined the LC-MS spectra of trypsin-digested Tf for −30-Da mass changes in peptide 366–380, represented as the fraction unmodified for each exposure time as described previously (5, 20). For isolated Tf a first order loss of the peptide 366–380 was accompanied by proportional increases of products shifted by −30 Da. The modification rate constant corresponding to the −30-Da products was 0.50 ± 0.02 s^{-1} for isolated Tf (Fig. 3*A*, *closed squares*) and was reduced over 80% to 0.08 ± 0.02 s^{-1} (Fig. 3*A*, *open squares*) in the case of the full-length Tf·TfR complex (Fig. 3*A*). Thus, based on both qualitative and quantitative mass spectrometry measures, we could specifically distinguish the oxidation of the acidic residues (based on the appearance of the −30-Da products) from oxidation of the other reactive site chains in the peptide (based on appearance of the +14- and +16-Da products, Table I).

Tandem MS was carried out on the +16-Da and −30-Da products of peptide 366–380 to determine the amino acids that experienced these mass changes as a function of oxidation (5, 20, 37). The tandem MS data indicate that Val-369 is the major contributor to the +16-Da modification (data not shown). However, the −30-Da oxidations derive from multiple residues throughput the peptide; thus Glu-367, Glu-372, Glu-375, and Asp-376 are indicated to suffer decarboxylation in isolated Tf (Supplemental Fig. 2) (29). Side chains of residues whose oxidation is suppressed by complex formation are explicitly indicated and colored in *purple* on the structure of Tf in Fig. 2*A*. The acidic residues experienced ~6-fold protection, whereas Val-369 was modestly protected. Based on this result, we reanalyzed our previously collected data from the C-lobe complexed to TfR (5) and found similar oxidative decarboxylation of peptide 366–380 for isolated C-lobe that was reduced over 80% in the complex. The reduced oxidation of these acidic residues within the C-lobe for both isolated C-lobe and full-length Tf are consistent with the interface predicted by cryo-EM studies (3). These data demonstrate that footprinting can detect the protection of acidic residues as a function of complex formation.

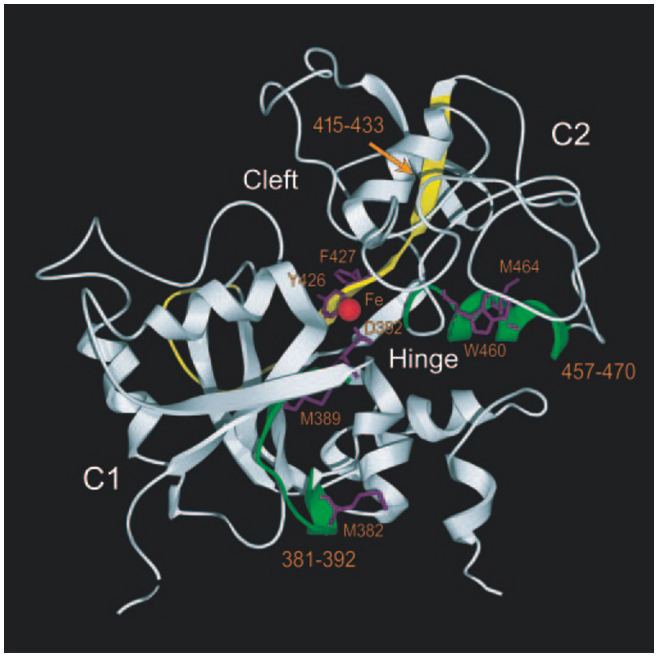

FIG. 4. **Allosteric changes in the structure of the Tf C-lobe.** Protein segments 381–392 and 457–470 are colored in *green*. Residues 381–392 from peptide 381–401 contain both of the probe residues for this peptide; thus the segment from 393–401 is not colored. Another peptide 415–433, which experienced significant protections in isolated Tf C-lobe bound to TfR (see text), is shown in *yellow*. The side chains of probe residues Met-382, Met-389, Phe-427, Trp-460, Met-464, and two residues bound to iron (Asp-392 and Tyr-426) are shown in *stick form*. Peptide 415–433 corresponds to one of the two hinge peptides located behind the iron atom connecting the C1 and C2 subdomains.

Tandem MS was carried out on the other Tf peptides (data not shown), indicating that Met-382 and Met-389 are the primary probe sites in peptide 381–401 (Fig. 2*A*). Met-389 is close to the iron-binding residue Asp-392 and is slightly accessible from the interdomain cleft (Fig. 4). Peptide 457–470 corresponds to a helix near the hinge running from the surface toward the iron binding site (Fig. 4). Trp-460 and Met-464 were determined to be the probe sites in this peptide. Probe residues in N-lobe peptide 51–88 include Val-60, Tyr-68, Tyr-71, Leu-72, and Pro-74, whereas those in N-lobe peptide 89–102 include Phe-94 and Tyr-96.

Protection of Helical Domain of TfR upon Tf Binding—The TfR homodimer consists of four regions: a large extracellular ectodomain, a stalk of about 30 Å between the ectodomain and the cell membrane, a transmembrane segment, and an N-terminal cytoplasmic domain. The transferrin-binding ectodomain (6) is comprised of three distinct subdomains: a protease-like domain proximal to the membrane, a helical domain responsible for dimer interface contacts, and a membrane-distal apical domain. Table I shows six peptides in the helical domain (sequence 607–760) that experienced protections of 80% or more as a function of TfR ectodomain binding to full-length Tf. The dose-response curve of TfR peptide 648–658 containing Arg-651 and Arg-655 is shown in Fig. 3*B*. In our previous study of C-lobe binding to receptor, peptides 614–623, 634–646, 647–651, and 733–760 of the receptor all experienced robust protections upon complex formation. The first three of these peptides correspond to two helices on the outside surfaces of the helical domains of the TfR dimer (Fig. 2*B*). Full-length Tf exhibits virtually identical protections for these four peptides compared with isolated C-lobe (5); thus isolated C-lobe and C-lobe within full-length Tf bind to TfR in a similar fashion, consistent with cryo-EM findings (3). The backbone positions of these peptides are colored in *green*, and the side chains of the probe residues within the peptides are shown in *purple* on the TfR ectodomain dimer in Fig. 2*B*. The probe sites for these peptides identified by tandem MS (data not shown) include Leu-619, Phe-621, Met-635, Trp-641, Tyr-643, and Phe-650 for the three peptides on the helical domain surface and residues Trp-740, Trp-754, and Phe-760 from the C-terminal tail.

Protection of Arginine Residues in TfR upon Complex Formation—Multiple arginine residues seen in the TfR helical domain include Arg-623, Arg-629, Arg-646, Arg-651, and Arg-655; Arg-646 is part of the highly conserved RGD sequence (646–648) essential for TfR binding (38). All of these arginine residues are within highly protected peptide sequences in the Tf·TfR complex. Recently using model peptides, we demonstrated that solvent-accessible arginine residues are susceptible to oxidation at the δ-position of the side chain leading to loss of the guanidine moiety and a characteristic mass change of -43 Da (28). Oxidation at the β or γ positions of the side chain results in alcohol or carbonyl formation (mass change of $+16$ or $+14$ Da) (28). Loss of the positive charge would impede the action of trypsin; thus peptides that suffer deguanidation should be refractory to trypsin cleavage at the oxidized sites. We thus digested TfR with endoproteinase Asp-N, revealing two peptides within the helical domain that exhibited significant protections as a function of complex formation (Table I). When the $+16$- and $+32$-Da modification products of peptide 631–647 were quantified using LC-MS, the peptide was observed to have a rate constant of modification of 2.6 ± 0.1 s^{-1} for isolated TfR compared with 0.2 ± 0.1 s^{-1} in the complex. These rate constants of modification are nearly identical to that observed from (partially overlapping) peptide 634–646 generated from a trypsin digestion. However, no -43-Da products were observed for this peptide, *e.g.* oxidation of Arg was not detected. Like peptide 631–647, peptide 648–658 showed protections upon Tf·TfR complex formation when $+16$- and $+32$-Da products were examined. A modification rate of 1.6 ± 0.1 s^{-1} was observed for isolated TfR (Fig. 3*B*, *closed circles*) compared with 0.23 ± 0.09 s^{-1} in the complex (Fig. 3*B*, *open circles*). These data are consistent with the results seen for the partially overlapping peptide 647–651. This peptide also exhibited characteristic -43-Da products that appeared with a rate constant of 0.63 ± 0.08 s^{-1} for isolated TfR (Fig. 3*B*, *closed squares*) that was reduced over 90% to 0.05 ± 0.08 s^{-1} in the complex (Fig. 3*B*, *open squares*).

It appears that the single arginine in peptide 631–647 (Arg-646) was not sufficiently reactive compared with other nearby reactive residues to be oxidized, or the δ-CH_2 of the Arg-646 side chain is not sufficiently accessible for modification. In contrast, peptide 648–658, which contained two highly solvent-accessible arginine residues with a total SASA of over 220 $Å^2$, was relatively easily oxidized. The specific protection of these arginine residues as a function of complex formation is consistent with the interface predicted by cryo-EM (3). These data demonstrate that footprinting can detect the protection of Arg as a function of complex formation.

DISCUSSION

The cryo-EM model of the Tf·TfR complex provided by Cheng *et al.* (3) allows quantitative predictions for specific side-chain interactions in the Tf/TfR interface. Using this cryo-EM data, we carried out solvent accessibility calculations of the Tf·TfR complex as well as for the Tf and TfR coordinates used to construct the model (see "Experimental Procedures"). These calculations are illustrated in Fig. 2, *C* (for Tf) and *D* (for TfR), where residue side chains that experience SASA decreases >15% upon complex formation are colored in *purple*. In the following sections, we compare these model predictions with the footprinting data shown in Fig. 2, *A* and *B*, to evaluate the contacts predicted by the model and to identify regions of potential allosteric change as a function of complex formation.

Footprinting Supports Transferrin Binding Sites Suggested by Cryo-EM Data—Peptide 366–380 corresponds to one β-strand and one α-helix on the surface of the C1 domain. In the cryo-EM model, the side-chain residues ranging from 367 to 372 are buried nearly 50% in the formation of the Tf·TfR complex including protected footprinting probe residues Glu-367, Val-369, and Glu-372 (Table I and Fig. 2*C*). Cryo-EM and mutagenesis data also indicate that peptide 349–365 is involved in TfR binding (3); unfortunately no MS signal was observed for this peptide in our experiments. Overall the data indicate a TfR binding region within the Tf C-lobe that includes sequences 349–380 (two helices and a β-strand). This region contains multiple charged residues on the Tf surface.

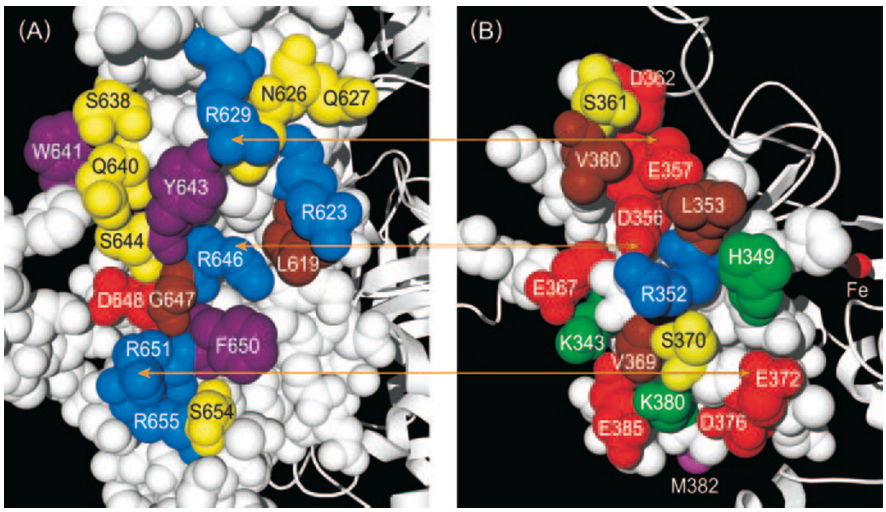

FIG. 5. **Binding model of Tf C-lobe/TfR interface.** Shown are the open-book view of the complementary structural epitopes on the TfR helical domain (*A*) and the Tf C-lobe (*B*). A complex charge-charge interaction network exists between the positively charged TfR helical domain and the highly negatively charged Tf C-lobe. The predicted contact regions are *linked*, and the residues are colored according to their physicochemical properties (*blue* for Arg; *red* for Asp and Glu; *green* for Lys and His; *yellow* for Asn, Ser, and Gln; *brown* for Val, Leu, Ile, and Gly; *purple* for Trp, Tyr, and Phe; and *magenta* for Met).

Within the Tf N-lobe, footprinting indicates that the probe residues within peptides 51–88 and 89–102 experienced conformational change as a result of complex formation (shown in *green* in Fig. 2*A*). The sequence protection pattern is consistent with the cryo-EM model (3), which predicts that side-chain residues 50–75 are within the contact interface. Specifically the five footprinting probe residues identified within peptide 51–88 (Val-60, Tyr-68, Tyr-71, Leu-72, and Pro-74) experience 65% reductions in solvent-accessible surface area in the formation of the complex. Meanwhile the cryo-EM model suggests that the N-lobe contacts the *receptor* between residues 123 and 126. We analyzed a tryptic peptide of sequence 122–128 (with probe residues of Tyr-123 and Trp-124) from this region of TfR (Table I and Fig. 2*B*) and found that the rate of oxidation was reduced about 40% upon complex formation, consistent with this contact as well. On the other hand, none of the residues within Tf peptide 89–102 corresponding to the hinge connecting the N1 and N2 subdomains of Tf are predicted in the cryo-EM model to be protected in the formation of the complex. Note that the backbone segment behind the N-lobe iron atom is colored *green* in Fig. 2*A* but not colored in Fig. 2*C*; these residues appear to be buried as a result of ligand-induced conformational change.

Allosteric Effects of Complex Formation Sequester Iron—Peptides 381–401 and 457–470 from the C-lobe are not predicted to be part of the binding interface; the probe residues within these two peptides experience allosteric conformational change as a result of complex formation (Fig. 4). All the probe residues in peptide 381–401 are within the sequence 381–392; thus only this part of the peptide sequence in colored in Fig. 4. Residues 381–392 correspond to the last turn of a helix near the binding site with a β-strand running from the surface to the protein core in the C1 domain. Peptide 457–470 (with Trp-460 and Met-464 as probe residues) in the C2 domain is on the opposite side of the C-lobe relative to the predicted interacting surface and corresponds to one helix running from the surface toward the iron binding site. The iron binding site is located close to the hinge, which consists of two antiparallel β-strands running behind the iron binding site connecting the C1 and C2 domains. One β-strand forming the hinge includes peptide 415–433, which has probe residue Phe-427 adjacent to iron ligand Tyr-426. This peptide is significantly protected in experiments where isolated Tf C-lobe is bound to TfR (5); unfortunately this peptide experiences ion suppression in the LC-MS experiments with full-length Tf. The observed protections, as well as protections observed for Met-389 near the iron-binding residue Asp-392, suggest subdomain movements and a tightening of the structure adjacent to the hinge resulting in sequestration of the iron atom.

For the N-lobe as well, footprinting data suggest closure around the iron atom as a function of receptor binding. Asp-63, one of the iron-binding ligands, is located at the same helix as protected probe residues Val-60, Tyr-68, Tyr-71, Leu-72, and Pro-74 (Fig. 2*A*). In addition, sequence 89–102 corresponds to one of the two β-strands of the N-lobe hinge; the primary probe residues Phe-94 and Tyr-96 are next to iron-binding ligand Tyr-95. The footprinting data point to a range of allosteric effects of receptor binding that stimulates increasing closure around the iron atoms beyond what is already present in the iron-bearing free protein; this helps provide a molecular explanation as to why receptor-bound diferric Tf releases iron significantly more slowly than free diferric Tf at the slightly alkaline extracellular pH (39, 40).

TfR Helical Domain Binding—The cryo-EM data indicate significant decreases in solvent-exposed surface area for Leu-619 (50%), Arg-623 (93%), Arg-629 (58%), Gln-640 (65%), Tyr-643 (83%), Arg-646 (91%), Phe-650 (77%), and Arg-651 (43%) as a function of complex formation. These residue side chains are colored *purple* in Fig. 2*D*. These predicted decreases in surface area are consistent with the protections for specific probe residues indicated in Table I. Helix 3 contains the RGD motif (residues 646–648) established to be critical for Tf binding (38). This binding site on TfR is also consistent with that found for hereditary hemochroma-

tosis protein binding to TfR, which competes with Tf for TfR binding (7, 41, 42). Mutagenesis studies also implicate this interface as mutations L619A, R629A, Y643A, and F650A decrease Tf binding (9, 41), whereas R651A and G647A abolish it (38). Protection at the flexible C-tail peptide 733–760 due to complex formation may involve changes in the dimer interface; the cryo-EM model does predict Tf contacts with TfR residues from 757 to 760. Although mutations such as F760A do not affect dTf binding at pH 7.4 (9), rearrangement of the flexible C-tail may assist in Tf binding by excluding solvent from the Tf-TfR binding area.

Charge-Charge Interactions in the TfR Binding Site of C-lobe—The most striking feature observed in the interface of the C-lobe within the TfR helical domain is the clustering of charged and polar residues on both sides at the interface. The footprinting data demonstrate the burial of acidic and basic residues within the C-lobe and the TfR helical domain, respectively. Fig. 5 is an "open-book" view of the Tf C-lobe/TfR interface. There are five positively charged arginine residues (Arg-623, Arg-629, Arg-646, Arg-651, and Arg-655), one negatively charged aspartate residue (Asp-648), and several other polar residues present within the TfR helical domain. Within the Tf C-lobe binding site, there are many negatively charged residues (Asp-356, Glu-357, Glu-367, Glu-372, Asp-376, and Glu-385) and four positively charged residues (Lys-343, His-349, Arg-352, and Lys-380) proximal to the Tf C-lobe binding site. The hydrophilic, charged nature of the interface strongly implies a cooperative charge-charge interaction network between the two proteins. Such networks involving two or more ion pairs are more common at complex interfaces and contribute more to protein stability than isolated ion pairs, which predominate in intramolecular interactions (43). The electrostatic interactions are enhanced by solvent exclusion and contacts of hydrophobic residues such as Leu-619, Tyr-643, and Phe-650 of TfR; these are implicated by footprinting to be buried in the interface. Based on the cryo-EM, hydrophobic residues such as Leu-353, Val-360, and Val-369 in Tf are likely buried as well, enhancing the exclusion of solvent.

Conclusion—The structural allostery and binding interface for the human serum Tf·TfR complex were identified using radiolytic footprinting and mass spectrometry. This work extended the use of such footprinting approaches to the examination of conformational changes for charged residues, and we confirmed a predicted ionic interaction between the Tf C-lobe and the receptor helical domain. In addition, the overall binding surfaces for C-lobe and N-lobe of transferrin and the corresponding interactions sites on the transferrin receptor predicted from cryo-EM were confirmed in solution. The footprinting data also revealed allosteric movements of the iron-binding C- and N-lobes of Tf that sequester iron as a function of complex formation resulting in tighter binding of the metal ion and promoting efficient ion transport during endocytosis.

Acknowledgments—We thank Dr. Thomas Walz of Harvard Medical School for kindly providing the coordinates of the Tf·TfR complex obtained from their cryo-EM studies. We thank Dr. Keiji Takamoto for help in making the figures. We also acknowledge the assistance of the Northeast Biodefense Consortium Proteomics Core at Yale University in custom peptide synthesis for this work.

* This work was supported by the National Institute for Biomedical Imaging and Bioengineering Biotechnology Center Program under Grant P41-EB-01979 and the NIDDK, National Institutes of Health under Grant R21-DK-69952. The costs of publication of this article were defrayed in part by the payment of page charges. This article must therefore be hereby marked "*advertisement*" in accordance with 18 U.S.C. Section 1734 solely to indicate this fact.

S The on-line version of this article (available at http://www.mcponline.org) contains supplemental material.

§ Both authors made equal contributions to this work and share the first authorship.

‖ To whom correspondence should be addressed: Case Center for Proteomics, Case Western Reserve University, BRB 930, 10900 Euclid Ave., Cleveland, OH 44106. Tel.: 216-368-4406; E-mail: mark.chance@case.edu.

REFERENCES

1. Richardson, D. R. & Ponka, P. (1997) The molecular mechanisms of the metabolism and transport of iron in normal and neoplastic cells. *Biochim. Biophys. Acta* **1331,** 1–40
2. Richardson, D. R. (2004) Mysteries of the transferrin-transferrin receptor 1 interaction uncovered. *Cell* **116,** 483–485
3. Cheng, Y., Zak, O., Aisen, P., Harrison, S. C. & Walz, T. (2004) Structure of the human transferrin receptor-transferrin complex. *Cell* **116,** 565–576
4. Baker, H. M., Anderson, B. F. & Baker, E. N. (2003) Dealing with iron: common structural principles in proteins that transport iron and heme. *Proc. Natl. Acad. Sci. U. S. A.* **100,** 3579–3583
5. Liu, R., Guan, J. Q., Zak, O., Aisen, P. & Chance, M. R. (2003) Structural reorganization of the transferrin C-lobe and transferrin receptor upon complex formation: the C-lobe binds to the receptor helical domain. *Biochemistry* **42,** 12447–12454
6. Lawrence, C. M., Ray, S., Babyonyshev, M., Galluser, R., Borhani, D. W. & Harrison, S. C. (1999) Crystal structure of the ectodomain of human transferrin receptor. *Science* **286,** 779–782
7. Lebron, J. A., West, A. P., Jr. & Bjorkman, P. J. (1999) The hemochromatosis protein HFE competes with transferrin for binding to the transferrin receptor. *J. Mol. Biol.* **294,** 239–245
8. Hall, D. R., Hadden, J. M., Leonard, G. A., Bailey, S., Neu, M., Winn, M. & Lindley, P. F. (2002) The crystal and molecular structures of diferric porcine and rabbit serum transferrins at resolutions of 2.15 and 2.60 Å, respectively. *Acta Crystallogr. Sect. D Biol. Crystallogr.* **58,** 70–80
9. Giannetti, A. M., Snow, P. M., Zak, O. & Bjorkman, P. J. (2003) Mechanism for multiple ligand recognition by the human transferrin receptor. *PLoS Biol.* **1,** E51
10. Zak, O. & Aisen, P. (2002) A new method for obtaining human transferrin C-lobe in the native conformation: preparation and properties. *Biochemistry* **41,** 1647–1653
11. Zak, O., Trinder, D. & Aisen, P. (1994) Primary receptor-recognition site of human transferrin is in the C-terminal lobe. *J. Biol. Chem.* **269,** 7110–7114
12. Tsai, C. J., Lin, S. L., Wolfson, H. J. & Nussinov, R. (1997) Studies of protein-protein interfaces: a statistical analysis of the hydrophobic effect. *Protein Sci.* **6,** 53–64
13. Ofran, Y. & Rost, B. (2003) Analysing six types of protein-protein interfaces. *J. Mol. Biol.* **325,** 377–387
14. Xu, D., Tsai, C. J. & Nussinov, R. (1997) Hydrogen bonds and salt bridges across protein-protein interfaces. *Protein Eng.* **10,** 999–1012
15. Honig, B. & Nicholls, A. (1995) Classical electrostatics in biology and chemistry. *Science* **268,** 1144–1149
16. Sinha, N. & Smith-Gill, S. J. (2002) Electrostatics in protein binding and function. *Curr. Protein Pept. Sci.* **3,** 601–614
17. Kumar, S. & Nussinov, R. (2002) Close-range electrostatic interactions in

proteins. *Chembiochem* **3,** 604–617
18. Guan, J.-Q. & Chance, M. R. (2004) in *Encyclopedia of Molecular Cell Biology and Molecular Medicine* (Meyers, R. A., ed) 2nd Ed., Vol. 4, pp. 549–568, Wiley-VCH, Weinheim, Germany
19. Guan, J.-Q., Almo, S. C. & Chance, M. R. (2004) Synchrotron radiolysis and mass spectrometry: a new approach to research on the actin cytoskeleton. *Acc. Chem. Res.* **37,** 221–229
20. Guan, J. Q., Vorobiev, S., Almo, S. C. & Chance, M. R. (2002) Mapping the G-actin binding surface of cofilin using synchrotron protein footprinting. *Biochemistry* **41,** 5765–5775
21. Gupta, S., Mangel, W. F., McGrath, W. J., Perek, J. L., Lee, D. W., Takamoto, K. & Chance, M. R. (2004) DNA binding provides a molecular strap activating the adenovirus proteinase. *Mol. Cell Proteomics* **3,** 950–959
22. Guan, J. G. & Chance, M. R. (2005) Structural proteomics of macromolecular assemblies using oxidative footprinting and mass spectrometry. *Trends Biochem. Sci.* **30,** 583–592
23. Nukuna, B. N., Sun, G. & Anderson, V. E. (2004) Hydroxyl radical oxidation of cytochrome c by aerobic radiolysis. *Free Radic. Biol. Med.* **37,** 1203–1213
24. Sharp, J. S., Becker, J. M. & Hettich, R. L. (2003) Protein surface mapping by chemical oxidation: structural analysis by mass spectrometry. *Anal. Biochem.* **313,** 216–225
25. Sharp, J. S., Guo, J. T., Uchiki, T., Xu, Y., Dealwis, C. & Hettich, R. L. (2005) Photochemical surface mapping of C14S-Sml1p for constrained computational modeling of protein structure. *Anal. Biochem.* **340,** 201–212
26. Maleknia, S. D., Wong, J. W. & Downard, K. M. (2004) Photochemical and electrophysical production of radicals on millisecond timescales to probe the structure, dynamics and interactions of proteins. *Photochem. Photobiol. Sci.* **3,** 741–748
27. Maleknia, S. D., Brenowitz, M. & Chance, M. R. (1999) Millisecond radiolytic modification of peptides by synchrotron X-rays identified by mass spectrometry. *Anal. Chem.* **71,** 3965–3973
28. Xu, G., Takamoto, K. & Chance, M. R. (2003) Radiolytic modification of basic amino acid residues in peptides: probes for examining protein-protein interactions. *Anal. Chem.* **75,** 6995–7007
29. Xu, G. & Chance, M. R. (2004) Radiolytic modification of acidic amino acid residues in peptides: probes for examining protein-protein interactions. *Anal. Chem.* **76,** 1213–1221
30. Xu, G. & Chance, M. R. (2005) Radiolytic modification of sulfur-containing amino acid residues in model peptides: fundamental studies for protein footprinting. *Anal. Chem.* **77,** 2437–2449
31. Xu, G., Kiselar, J., He, Q. & Chance, M. R. (2005) Secondary reactions and strategies to improve quantitative protein footprinting. *Anal. Chem.* **77,** 3029–3037
32. Xu, G. & Chance, M. R. (2005) Radiolytic modification and reactivity of amino acid residues serving as structural probes for protein footprinting. *Anal. Chem.* **77,** 4549–4555
33. Zak, O. & Aisen, P. (2003) Iron release from transferrin, its C-lobe, and their complexes with transferrin receptor: presence of N-lobe accelerates release from C-lobe at endosomal pH. *Biochemistry* **42,** 12330–12334
34. Zak, O. & Aisen, P. (2003) A poly-His tag method for obtaining the C-terminal lobe of human transferrin. *Protein Expr. Purif.* **28,** 120–124
35. Tsodikov, O. V., Record, M. T., Jr. & Sergeev, Y. V. (2002) Novel computer program for fast exact calculation of accessible and molecular surface areas and average surface curvature. *J. Comput. Chem.* **23,** 600–609
36. Maleknia, S. D., Ralston, C. Y., Brenowitz, M. D., Downard, K. M. & Chance, M. R. (2001) Determination of macromolecular folding and structure by synchrotron x-ray radiolysis techniques. *Anal. Biochem.* **289,** 103–115
37. Kiselar, J. G., Janmey, P. A., Almo, S. & Chance, M. R. (2003) Structural analysis of gelsolin using synchrotron protein footprinting. *Mol. Cell. Proteomics* **2,** 1120–1132
38. Dubljevic, V., Sali, A. & Goding, J. W. (1999) A conserved RGD (Arg-Gly-Asp) motif in the transferrin receptor is required for binding to transferrin. *Biochem. J.* **341,** 11–14
39. Bali, P. K. & Aisen, P. (1991) Receptor-modulated iron release from transferrin: differential effects on N- and C-terminal sites. *Biochemistry* **30,** 9947–9952
40. Bali, P. K., Zak, O. & Aisen, P. (1991) A new role for the transferrin receptor in the release of iron from transferrin. *Biochemistry* **30,** 324–328
41. West, A. P., Jr., Giannetti, A. M., Herr, A. B., Bennett, M. J., Nangiana, J. S., Pierce, J. R., Weiner, L. P., Snow, P. M. & Bjorkman, P. J. (2001) Mutational analysis of the transferrin receptor reveals overlapping HFE and transferrin binding sites. *J. Mol. Biol.* **313,** 385–397
42. Bennett, M. J., Lebron, J. A. & Bjorkman, P. J. (2000) Crystal structure of the hereditary haemochromatosis protein HFE complexed with transferrin receptor. *Nature* **403,** 46–53
43. Musafia, B., Buchner, V. & Arad, D. (1995) Complex salt bridges in proteins: statistical analysis of structure and function. *J. Mol. Biol.* **254,** 761–770